Draft version March 9, 2024
Typeset using LaTeX **preprint2** style in AASTeX62

ETA CARINAE'S DECLINING OUTFLOW SEEN IN THE UV, 2002-2015*

Kris Davidson,[1] Kazunori Ishibashi,[2] John C. Martin,[3] and Roberta M. Humphreys[1]

[1]*Minnesota Institute for Astrophysics, 116 Church St SE, University of Minnesota, Minneapolis, MN 55455*
[2]*Graduate School of Science, Nagoya University, Nagoya, 464-8602, Japan*
[3]*Barber Observatory, University of Illinois, Springfield, IL, 62703*

ABSTRACT

Existing HST UV data offer many previously neglected clues to η Car's behavior since 2000. Here we examine a subset of observations with diverse results. (1) The star's rapid change of state is confirmed by major changes in UV absorption lines, circumstellar extinction, and other features. (2) N III] λ1750 is one of the two most luminous emission features in η Car's observable spectrum, comparable to Hα. This and other semi-forbidden lines are useful because they have no P Cyg absorption. (3) N III] multiplet ratios provide the first direct diagnostic of gas densities in η Car's outflow. They strongly suggest that high-excitation lines originate in condensations within the colliding-wind shocked region. The parameters imply that published models have not adequately represented the essential small size scales. (4) In 2002-2004, a very large amount of N III] emission had anomalous Doppler velocities from +400 to +1200 km s^{-1}. This is a mystery; we conjecture that it may have resulted from a burst of mass ejection in the 2003.5 periastron event. Various other effects are also difficult to explain and merit further investigation.

1. INTRODUCTION

Eta Carinae's unique role in stellar astrophysics arises from three circumstances:

1. Its primary star is the only supernova impostor or giant-eruption survivor that can be studied in detail.

2. Its dense wind has changed dramatically in the past 20 years.

3. Extraordinary effects occur at 5.5-year intervals during periastron passages of a companion star.

Item 1 is fundamental because the basic instability remains mysterious after many years of study; while 2 and 3 can provide clues to the star's internal recovery following its Great Eruption observed in 1830–1860. For general information, see reviews by many authors in Davidson & Humphreys (2012).

The Hubble Space Telescope (HST) revolutionized this topic, because all ground-based photometry and spectroscopy of η Car is severely contaminated by ejecta at $r \sim$ 300-1500 AU, seen less than 0.5 arcsec from the star. (See Fig. 1 in Davidson et al. 2015, Fig. 5 in Davidson et al. 1995, and discussions in Mehner et al. 2011b, 2012.) The Space Telescope Imaging Spectrograph (STIS) has played the largest role in this story, using wavelengths longer than 250 nm. In this paper we explore

* Based on observations made with the NASA/ESA Hubble Space Telescope, which is operated by the Association of Universities for Research in Astronomy, Inc., under NASA contract NAS 5-26555.

FUV wavelengths between 160 and 230 nm – a spectral region that is physically different as noted in §3 below.

For stellar astrophysics the *major* problem of η Car is the nature of its instability and its Great Eruption (see Davidson 2012 for a semi-theoretical account). In that sense, the most crucial development in this topic since 2000 has been the rapid trend of changes in the star. Recent publications tend to focus instead on geometries of the colliding winds, the binary orbit, and other matters that are less fundamental (e.g., Gull et al. 2016; Richardson et al. 2016; Teodoro et al. 2016; Weigelt et al. 2016 and many others). That is true of §4 and §5 in this paper as well, but our motivation differs. Rather than viewing the complicated gas flows as the main topic in their own right, we hope that their secular changes will eventually lead to information about the disequilibrium structure of the post-eruption star. Observed long-term spectroscopic *trends* are therefore critical. The goal of linking them to the star's internal structure has not been approached yet, but no other known object can offer comparable views into a supernova impostor.

Here we explore a particular subset of UV observations, selected by a criterion noted in §2. They contain a wide variety of results. Some of these relate to η Car's secular trend, while others involve the morphology and physics of gas flows in the system. Several phenomena were not recognized earlier, and appear difficult to explain.

Section 2 below is a brief description of the data set, and Section 3 is an overview of the rapidly growing UV brightness levels. In Section 4 we focus on the extraordinarily bright N III] λ1750 multiplet which has several important implications. In Section 5 we note the potential importance of other semi-forbidden lines, and Section 6 contains an account of a few especially suggestive absorption features. Finally,

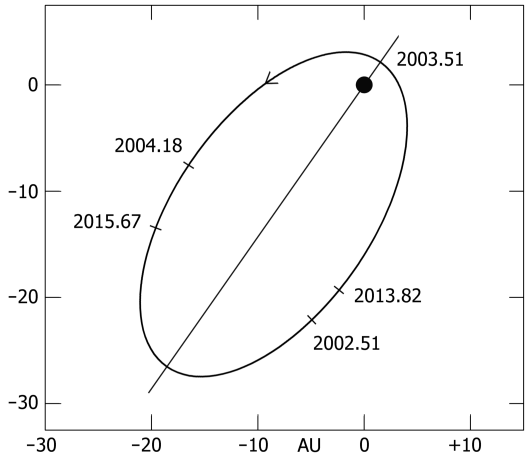

Figure 1. The 5.54-year orbit of η Car's companion star, with dates of UV observations discussed in this paper. In most models our line of sight passes upward in the figure, inclined 45° from the orbital plane, but some authors advocate the opposite direction. Here we assume eccentricity 0.85, see refs. cited in the text.

Section 7 is an attempt to summarize the resulting situation.

2. STIS/MAMA/UV OBSERVATIONS AND DATA REDUCTION

HST/STIS has played a unique role in our knowledge of η Car for three reasons: (1) As noted above, it can separate the central star from the surprisingly bright ejecta located 0.1–0.5 arcsec away. (2) It allows UV observations. (3) It also provides unrivaled data homogeneity since 1998, immune to atmospheric effects and far more reproducible in spatial coverage than ground-based data.

Here we are interested in secular trends at $\lambda < 2400$ Å, observable with the STIS/MAMA detectors. In order to minimize periodic variations related to the 5.54-year orbit, we chose pairs of observations that occurred at similar orbital phases. There are only two such pairs, shown in Figure 1. One of them includes $t =$ 2002.51 and 2013.82, about a year before periastron; while the other pair occurred at 2004.18 and 2015.67, after periastron. Eta Car was not

Table 1. Times of HST/MAMA echelle observations used in this paper

Year	Calendar	MJD	Phase[a]	Program[b]
J2002.51	2002-07-05	52459.9	0.8136	9337
J2003.51	2003-07-05	52825.0	0.9941	9973
J2004.18	2004-03-06	53070.3	0.1153	9973
J2013.82	2013-10-27	56591.8	0.8561	13377
J2015.67	2015-09-02	57267.3	0.1900	13789

[a]Phase in the 5.54-year orbit, with nominal period 2023.0 days and zeropoint at J1998.000. Periastron is ill-determined but most likely occurs in the phase range 0.988–0.998.

[b]HST/GO program number. P.I.'s were K. Davidson in 2002-2004 and A. Mehner in 2013-2015.

observed with STIS/MAMA in the intermediate years 2005–2012. Table 1 lists the four selected observations, plus another that occurred during the 2003.5 spectroscopic event near periastron.

The STIS/MAMA/FUV detector sampled wavelength range 1300–1700 Å with echelle grating E140M, and the NUV detector sampled 1610–2360 Å with grating E230M. Spectral resolution was equivalent to $\Delta v \sim 10$ km s^{-1}, much narrower than most of the spectral features. In 2002-2004 the integration times were around 2000 s with E140M, and 3500 s with E230M. Eleven years later η Car's brightening allowed shorter integrations, about 1000 s and 800 s respectively. Since the resulting data had many thousands of counts per Å at most wavelengths, statistical noise was much smaller than other sources of uncertainty that will be obvious below. The spectrograph aperture size was 0.2×0.2 arcsec for E140M, and 0.2×0.3 arcsec for E230M. These were near the maximum size that can exclude emission from nearby ejecta. On the other hand, Hillier et al. (2006) noted that we must include as much as possible of a UV scattering halo whose effective diameter exceeded 0.1 arcsec in 2002-2004. Therefore the chosen aperture size was a reasonable compromise.

Our data reduction methods essentially followed the standard STScI CALSTIS pipeline processing. Spectral extractions presented in this paper were performed with the full aperture width and standard pipeline aperture corrections. Strictly speaking the aperture corrections may be unreliable for η Car due to the noticeable extent of its emission; but there is not enough information to do much better. Judging from the near-absence of very narrow emission lines, and from spatial structure within the aperture width, the nearby slow-moving ejecta did not appreciably contaminate these data.

Orbital positions at the times of these observations are sketched in Figure 1. According to most authors we view the orbit from below the bottom edge of the figure and roughly 45° out of its plane, but a nearly opposite line of sight has also been proposed, see refs. in Kashi & Soker (2016). As noted in §4 below, high-excitation species such as He^+ and N^{++} should occur in and near a shocked zone where the two winds collide, between the two stars. Concerning the orbit parameters, see Davidson et al. (2001, 2017), §6.2 in Mehner et al. (2011b), and references therein. None of our conclusions depend on their precise values.

Regarding "phase" in the 5.5-year orbital cycle, we use the definition adopted 15 years ago for the η Car Treasury Project: period = 2023.0 days exactly, and phase is zero (or alternatively an integer) at MJD 56883.0 = 2014 August 14, MJD 54860.0 = 2009 January 29, etc. This system has been used in most accounts of HST data on the central star, and reasons for it are outlined in an Appendix in Mehner et al. (2011b).

Quoted wavelengths are in vacuum, and Doppler velocities are heliocentric. Eta Car's heliocentric systemic radial velocity is probably

in the range 0 to −20 km s^{-1} (Davidson et al. 1997).

3. THE UV JUNGLE, AND DIMINISHING EXTINCTION

Figure 2 shows η Car's UV spectrum at $t = 2015.67$. It is far more complex than the spectral region $\lambda > 3500$ Å, cf. tracings in Davidson et al. (1995, 1999a); Humphreys et al. (1999); Hillier et al. (2001); Humphreys & Martin (2012); Najarro & Hillier (2012). The UV continuum level cannot be clearly identified. Ebbets et al. (1997), Walborn (1999), and Hillier et al. (2001) compared η Car's FUV spectrum to various known single-star winds, but later it was recognized that the hot companion star photoionizes some of the observed gas – see §6 in Humphreys et al. (2008), and §4 below. The secondary star itself is relatively faint at wavelengths examined here (Mehner et al. 2010a).

One might hope that the hundreds of features in η Car's UV spectrum can be analyzed via numerical simulations (Hillier et al. 2001; Groh et al. 2012a; Madura et al. 2013; Clementel et al. 2015). However, there are too many asymmetric emitting regions and small-scale processes, with far too many free parameters, for a reliable model with any set of computer codes available now or in the near future (see §4.3 and §7.2 below). We therefore concentrate on spectral features that depend chiefly on just a few physical processes.

3.1. *A minor paradox*

First, though, note that most features in this wavelength range do not depend on the same parameters as the violet-to-red spectrum. Mehner et al. (2010b) found that η Car's Fe II emission lines at $\lambda > 4000$ Å weakened by factors of 2–5 between the years 2000 and 2010, relative to the continuum. In our UV data, however, the Fe II forest appeared roughly the same in 2015 as it did in 2002. This difference is not a contradiction, for the following reasons.

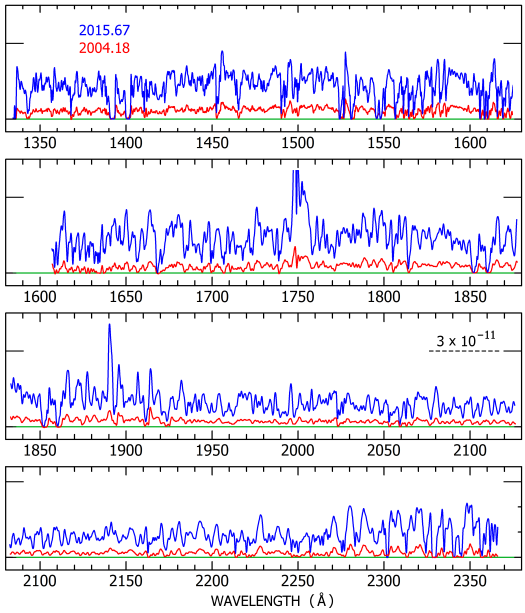

Figure 2. UV spectrum observed at 2015.67, and also at 2004.18 to show the apparent brightening. Horizonal marks indicate flux level $f_\lambda = 3 \times 10^{-11}$ erg cm^{-2} s^{-1} Å^{-1}, not corrected for extinction. The spectral features visible here are nearly all real, since the statistical noise level is too small to discern at this scale.

Fe II has about three dozen levels with $E_i < 3$ eV, mostly well populated because they are metastable. They produce a few hundred UV absorption lines with substantial optical depths in η Car's *outer* wind, at $r \sim 50$–200 AU. A typical absorption event is followed by re-emission either in the same line, or in another UV line with $\lambda < 3000$ Å. (Longer-wavelength transitions have much smaller probabilities.) Many scattering events – really absorption and re-emission – may occur before the photon escapes. Consider first a simplified case with only one spectral line. In a stellar wind, it produces a P Cyg profile of the pure-scattering type: some energy is removed from a narrow wavelength interval and transferred to slightly longer wavelengths. If the line-center optical depth τ_0 is larger than about 1.5, then the amplitude and

width of the resulting line profile do not strongly depend on the actual value of τ_0. In other words, if more than (say) four scattering events occur before photon escape, then the specific number of them has only a weak influence on the line's apparent strength. Thus *a major change in the gas density does not greatly alter the appearance of the spectral feature.* The line's quantitative details are affected, but not its basic nature.

In reality each Fe II absorption event may be followed by re-emission in a different UV transition, but this fact merely re-distributes the scattering among a limited set of spectral lines, and the pure-scattering P Cyg concept remains valid for their average. In summary, we should not expect a conspicuous change in the general appearance of η Car's ultraviolet Fe II forest; that would happen only if nearly all of the line optical depths τ_0 fall below 1.5. The same remarks apply to Ni II and other complex species.

Sometimes the scattering sequence ends with a relatively unlikely non-UV decay, producing a photon with $\lambda > 4000$ Å which escapes more easily. This has a specific probability of occurring after each UV absorption event, so the resulting amount of longer-wavelength emission is roughly proportional to the average number of UV absorption events that occur before a re-emitted photon escapes. Thus a higher UV optical depth implies relatively more photons with $\lambda > 4000$ Å. Consequently the violet-to-red emission lines strongly depend on the Fe II density, unlike the UV lines. This is why the features noted by Mehner et al. (2010b) weakened dramatically without a proportionate change in the UV spectrum.

3.2. *The UV brightening*

The flux levels in our UV data increased by factors of about 5 between 2002 and 2015, see below. Since η Car is fairly close to the Eddington Limit, it cannot brighten intrinsically by such a factor. Hence the observed brightening must indicate a rapidly declining circumstellar extinction. Two complications must be acknowledged, however. First, what we call "extinction" may involve a scattering halo at $r \sim 100$ to 500 AU (Hillier et al. 2006), not just line-of-sight obscuration. The halo is correlated with the circumstellar outflow density. Secondly, the star's SED may have changed by a small amount. In order to simplify the narrative, here we report the observed trend as though it were simple line-of-sight extinction by dust; future theoretical studies can make suitable corrections.

Table 2. Quasi-continuum Flux Levels[a]

Date	1733Å	1777Å	1968Å	2072Å	2000-2200Å[b]
2002.51	3.2	3.2	2.1	2.0	1.80
2004.18	2.9	3.5	2.8	2.5	1.90
2013.82	13.0	12.8	8.9	7.5	6.48
2015.67	16.8	17.0	12.2	11.3	8.49

[a] f_λ expressed in units of 10^{-12} erg cm^{-2} s^{-1} Å^{-1}, not corrected for extinction. The four narrow samples are each 4 to 7 Å wide.

[b] The broad 2000-2200 Å interval includes many absorption lines.

As quasi-continuum samples, we adopt four narrow wavelength intervals which appear as local plateaus in f_λ; see Table 2. These provide meaningful flux measures even if they do not represent a true continuum, because (1) they had similar plateau-like appearances at each of the observation dates, and (2) their relative flux ratios remained consistent through the 2002, 2004, 2013, and 2015 observations. These f_λ samples are plotted in Figure 3. Table 2 and most of our figures do not include corrections for extinction, because A_λ is only vaguely known for this object. A primary goal of the next few paragraphs is to estimate the extinction.

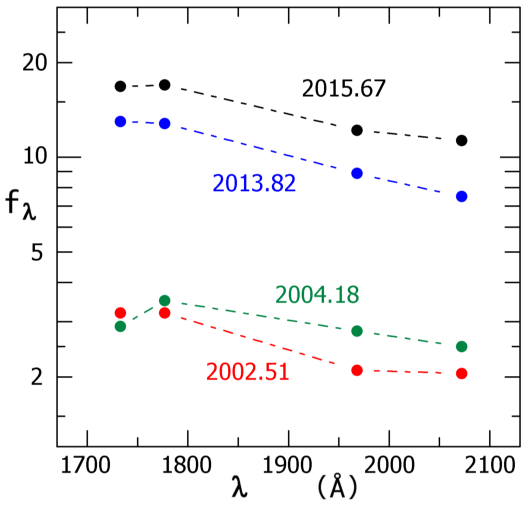

Figure 3. Observed flux at four quasi-continuum wavelengths listed in Table 2, not corrected for extinction. Here the unit for f_λ is 10^{-12} erg cm^{-2} s^{-1} Å^{-1}.

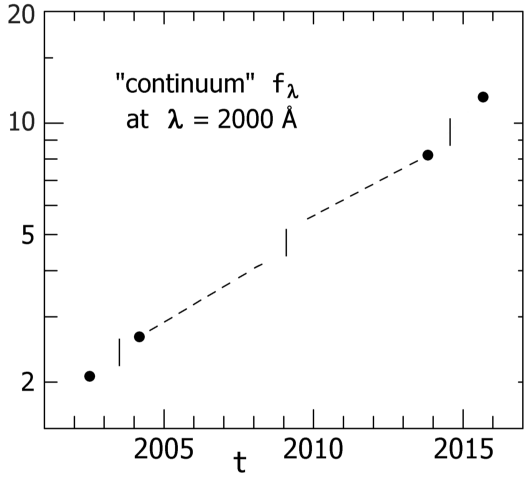

Figure 4. Progressive increase in apparent flux, an average of the 1968 Å and 2072 Å data listed in Table 2. The unit of f_λ is 10^{-12} erg cm^{-2} s^{-1} Å^{-1}. Vertical marks indicate the times of periastron events in 2003, 2009, and 2014. A conjectural discontinuity in 2009 is consistent with HST photometry at longer wavelengths (Martin et al. 2018, in preparation).

The uncertainties in Table 2 are not statistical, but likely error sizes can be be estimated with a few assumptions. Suppose that the intrinsic fluxes at 1733, 1777, 1968, and 2072 Å were constants, and that changes of extinction had the local wavelength dependence $\Delta A_\lambda \propto \lambda^\alpha$ in the range 1700-2100 Å, with a constant value of α. Given the 16 data points, one can calculate a best-fit model that has eight parameters: three numbers that describe the intrinsic fluxes relative to each other, values of ΔA_λ(2000 Å) at four observation times, and α. (The best-fit α turns out to be about -0.5.) Then we can deduce typical errors from differences between the measured f_λ values and the model, allowing for its degrees of freedom. Based on this method, the r.m.s. error in each listed f_λ value is roughly $\pm$10% or $\pm$0.11 magnitude, much larger than the statistical count-rate errors. This probably involves real fluctuations in the spectrum, and the largest deviations occurred at the shortest wavelength 1733 Å.

As noted above, the five-fold increase in Figure 3 represents primarily a decrease in extinction. Most likely the rate of mass outflow along our line of sight has diminished, so less dust is being formed at $r \sim$ 100 to 400 AU (Martin et al. 2006b, 2010; Humphreys & Martin 2012; Davidson et al. 1999b). Figure 4 shows the trend for an average of the fluxes centered at $\lambda \approx$ 1968 and 2072 Å. The time-averaged rate of brightening from 2002 to 2015 was between 12% and 16% per year at all four wavelengths in Table 2, with an overall average of 13.8% per year or 0.14 $\pm$ 0.01 magnitude y^{-1}. (Here the quoted error may be doubtful because it is based on the f_λ uncertainty estimated above, where normal statistics do not apply.) The brightening rate was approximately proportional to $\lambda^{-0.5}$ in the sampled range 1733–2072 Å. "Normal" extinction increases with λ in this range (Cardelli et al. 1989), but η Car's extinction law is notoriously peculiar with large grains and nitrogen-rich gas, see refs. in Walborn (2012) and Davidson & Humphreys (1997). Moreover, the "UV halo" effects mentioned earlier may af-

fect the wavelength dependence. These remarks apply only to recently formed outflowing dust within 1000 AU of the star.

Other wavelength samples give similar rates of change. For instance, the 2000-2200 Å flux in Table 2 is a simple average across that broad interval, including many spectral lines. It shows an average brightening rate of 0.13 magnitude per year.

We can estimate the total UV extinction, based on the following assessment of intrinsic brightness. Since η Car's photospheric temperature is probably in the range 15000–25000 K (Davidson 2012), most of its emergent radiation should be in the wavelength range 1000–3000 Å. Scattering effects noted by Hillier et al. (2006) cannot shift a major fraction of the integrated flux out of this range. For simplicity, first consider a Planck distribution with a Lyman cutoff near 912 Å. If Φ_{2000} denotes the intrinsic value of λf_λ at $\lambda = 2000$ Å (i.e., what we would see in the absence of extinction), and F is the total intrinsic energy flux $\int f_\lambda d\lambda$ including all wavelengths, then $0.5F < \Phi_{2000} < 0.8F$ for any Planck temperature in the range noted above. Further details are too lengthy to explore here, but $\Phi_{2000} \approx 0.6F$ appears probable, within a factor of 1.6 or so, for a realistic SED with free-free emission, a scattered halo, and other effects. Given the standard luminosity $L \approx 4\times10^6\ L_\odot$ for the primary star and $D \approx 2.3$ kpc, we thus expect $\Phi_{2000} \sim 1.5\times10^{-5}$ erg cm^{-2} s^{-1} and $f_\lambda(2000\ \text{Å}) \sim 7.5\times10^{-9}$ erg cm^{-2} s^{-1} Å^{-1} without extinction. A factor-of-two error in this quantity would alter the extinction A_λ derived below by only about 10%.

In 2015 the apparent $f_\lambda(2000$ Å) was smaller than the above value by a factor of about 630 (Table 2), implying 7.0 magnitudes of extinction. Since η Car's *interstellar* extinction amounts to roughly 3.3 magn at 2000 Å,[1] the circumstellar extinction in 2015 was evidently about 3.7 magn at 2000 Å with an informal pseudo-sigma uncertainty of the order of ±0.6 magn. Thirteen years earlier the star appeared 1.8 magn fainter (Fig. 4), so the UV circumstellar extinction decreased by roughly 33%. Note, however, that an unknown fraction of the "circumstellar" extinction occurs in older ejecta located at $r \sim 10^3$ to 10^4 AU, which would have changed at a much smaller rate due to expansion. Hence, allowing for normal uncertainties, the current dust-formation rate appears to have fallen by more than 30% between 2002 and 2015. Extrapolating back to 1998 when η Car's rapid brightening was first noticed, we conclude that *the dust-formation rate along our line of sight decreased by at least 35%* and probably more, perhaps about 50%.

3.3. *Related issues*

Part of the measured brightening may involve a decrease in the size of a UV scattering halo (Hillier et al. 2006); but that too would indicate a diminished outflow density, so the basic implication is not materially altered. (The STIS/MAMA 0.2-arcsec aperture included most of the halo according to Hillier's Figure 15.) One might attribute the trend to a destruction of dust grains, rather than a decreased rate of grain formation; but that would require a change in the UV output or some other characteristic of the star, which would alter the mass flow rate as well. As Davidson et al. (1999b) explained, the observed trend has been far too rapid to be a mere consequence of expansion or sideways motion of pre-existing dust. That paper also noted reasons to suspect that the effect is less dramatic in some other directions from the star. Incidentally, outflowing gas reaches

[1] $A_V \approx 1.5$ (Davidson & Humphreys 1997) with an $R = 4$ Cardelli law (Cardelli et al. 1989).

the dust-formation region about two years after leaving the star.

In principle the temporal baseline can be extended about a decade earlier, because η Car was observed in 1991–1997 with HST's Faint Object Spectrograph (FOS) and Goddard High Resolution Spectrograph (GHRS) (Davidson et al. 1995; Humphreys et al. 1999; Ebbets et al. 1997). One datum is highly relevant here: at $t = 1991.62$, near the same orbital phase as 2002.51 and 2013.82, the average apparent f_λ(1450-1700 Å) was *probably* about 7×10^{-13} erg cm^{-2} s^{-1} Å^{-1} (Davidson et al. 1995). We emphasize "probably" because those early FOS data required unorthodox analysis to achieve sufficient spatial resolution. Relative to Table 2, *one deduces a UV brightening rate of roughly 0.13 magn y^{-1} from 1991 to 2002* – practically the same as in 2002–2015.

This result is moderately surprising for two reasons: (1) the accelerated brightening in ground-based photometry began several years after 1991; and (2) in the early 1980's, the star appeared definitely brighter than the Weigelt knots (Weigelt & Ebersberger 1986). Since their energy budget and line ratios indicate much less extinction than for the star (Hamann 2012; Davidson et al. 1997; Davidson & Humphreys 1997), a naive extrapolation of the 1998-2015 trend back to 1984 would make the star no brighter than the knots at that time, even at far-red wavelengths. *The FOS and GHRS data, and also the International Ultraviolet Explorer (IUE) observations of η Car in the 1980's, merit new examinations relative to the STIS data* – a task beyond the scope of this paper.

Concerning the FUV quasi-continuum level (Fig. 2), one must be careful with the word "photosphere" in a diffuse flow. In order to be physically meaningful as well as consistent with traditional usage, a photosphere should be the region that determines the emergent photon energy distribution. In a hot atmosphere or wind, this is the thermalization depth where $(3\,\tau_{\rm tot}\,\tau_{\rm abs})^{1/2} \approx 1$. If η Car has $\dot{M} \gtrsim 3 \times 10^{-4}\ M_\odot$ y^{-1}, then its photosphere defined this way is located in the wind rather than near the star's surface (Davidson 1987).[2] The single-star wind model described by Hillier et al. (2001), for example, had a characteristic photosphere temperature somewhat above 15000 K. The classical effective temperature $T_{\rm eff}$ has no physical significance in a diffuse configuration.

Table 3. The N III] λ1750 Multiplet[a]

λ_0 (Å)	$J_{\rm lower}$[b]	$J_{\rm upper}$[b]	A_{ji} (s^{-1})
1746.823	1/2	3/2	8.8
1748.646	1/2	1/2	346.8
1749.674	3/2	5/2	266.0
1752.160	3/2	3/2	60.2
1753.995	3/2	1/2	361.5

[a]See Bell et al. (1995) and Stafford et al. (1994).

[b]Lower and upper terms are $2s^2 2p\ ^2$P$^{\rm o}$ and $2s2p^2\ ^4$P respectively.

4. EXTREMELY LUMINOUS N III] EMISSION

The secondary star in η Car has $T_{\rm eff} \sim 40000$ K (Mehner et al. 2010a), hot enough to photoionize helium in some parts of the primary star's wind. Nitrogen is more abundant there than carbon plus oxygen (Davidson et al. 1986), and tends to be doubly ionized in a zone of He$^+$. Therefore semi-forbidden N III] λ1750 emission (Table 3) is a very strong coolant in

[2] Calculations by Owocki & Shaviv (2016) agree in their essentials with the simplified view in Davidson (1987), if we allow for modern opacity values. Their discussion seems to imply otherwise, largely because they quoted only textual comments rather than the quantitative temperatures shown in Davidson's Figure 1.

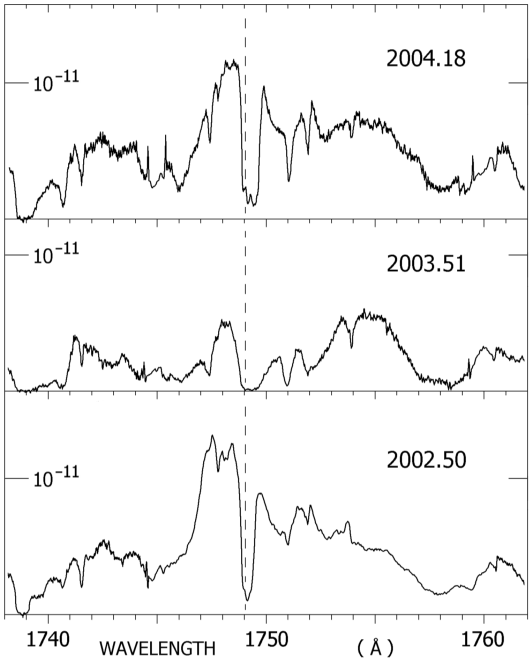

Figure 5. N III] λ1750 emission observed in 2002-2004. Horizontal marks indicate $f_\lambda = 10^{-11}$ erg cm^{-2} s^{-1} Å^{-1}, not corrected for extinction. A vertical dashed line marks -500 km s^{-1} for the Ni II λ1751.9 absorption line. The middle panel is atypical because it represents a brief "spectroscopic event" at periastron.

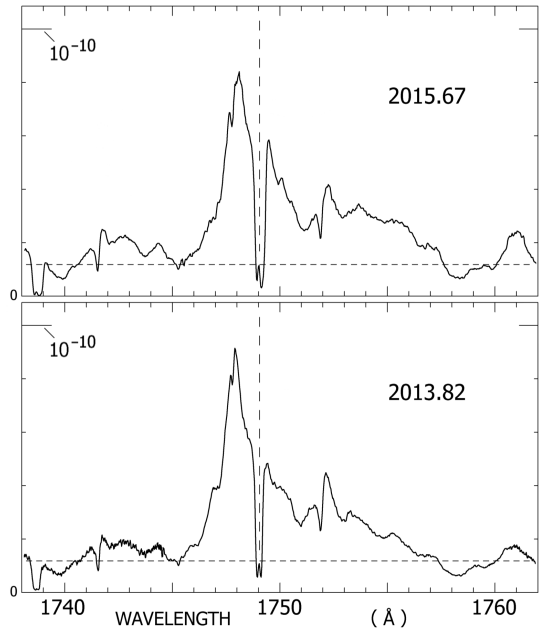

Figure 6. N III] λ1750 emission in 2013-2015. Horizontal marks indicate $f_\lambda = 10^{-10}$ erg cm^{-2} s^{-1} Å^{-1}, not corrected for extinction. A vertical dashed line marks -500 km s^{-1} for the Ni II λ1751.9 absorption line.

the He$^+$ zone. Three attributes together make this feature unique in η Car's spectrum: (1) It is fundamentally strong as just noted; (2) it has a rather high excitation energy; and (3) being semi-forbidden, it has no P Cyg absorption or other self-absorption.

The N III] multiplet provides evidence for a long-standing question, the location of the photoionized He$^+$ region within the wind structure. It also reveals some fresh problems. Throughout the following discussion, we invoke numerous conventional parameters for the η Car system. For explanations of them and references, see the review articles in Davidson & Humphreys (2012).

4.1. *The N III] luminosity*

N III] emission, like the He I recombination lines, does *not* depend primarily on the amount of material present. Instead it represents the EUV luminosity of the hot secondary star. Most photons with $h\nu \gtrsim 25$ eV are absorbed by He^0 $\rightarrow$ He$^+$ events somewhere in the gas flow, and most of their energy flux is then recycled to $h\nu \lesssim 10$ eV by recombination, N III] emission, and other cooling processes (Humphreys et al. 2008). To a first approximation, the N III] luminosity is thus independent of the gas density distribution. The line profile, however, depends on flow velocities of the EUV-absorbing material. Figures 5 and 6 show the observed profile of N III] λ1750 in 2002-2015. The very different-looking middle panel in Figure 5 represents the 2003.5 periastron event which was too complicated to discuss here (Davidson & Humphreys 2012; Martin et al. 2006a; Mehner et al. 2011b, 2015).

The luminosity of N III] emission can be estimated as follows. For a reason noted in §4.5, let us focus on the data at $t = 2013.82$. The integrated apparent flux was then F(N III]) $\approx 2.4 \times 10^{-10}$ erg cm^{-2} s^{-1}, continuum subtracted and not corrected for extinction. Here we interpolated across the absorption lines via a model in §4.2 below, and the informal pseudo-sigma uncertainty is roughly ±15%. Extinction at 1750 Å amounted to 7.7 ± 0.7 magnitudes (§3.2 above, adapted to 2013 rather than 2015). Hence the flux without extinction would be F_0(N III]) $\approx 3 \times 10^{-7}$ erg cm^{-2} s^{-1}. This implies luminosity L(N III]) $\approx 2 \times 10^{38}$ ergs s^{-1} $\approx 5 \times 10^4$ $L_\odot$, which is enormous for a stellar-wind emission feature. The uncertainty is a factor of about 2.

This value exceeds the total kinetic energy outflow of the wind, and a single-star wind produces far less N III] emission (Hillier et al. 2001, 2006). Hence this feature is almost certainly powered by ionizing radiation from the hot secondary star, perhaps supplemented by an effect noted in §6 of Humphreys et al. (2008). But the energy budget seems problematic in light of the following facts:

1. The 40000 K companion star discussed by Mehner et al. (2010a) radiates less than 10^5 $L_\odot$ at helium-ionizing photon energies $h\nu > 24.6$ eV.
2. Even though N III] λ1750 emission may be the strongest individual cooling mechanism in a He$^+$ zones, other processes should account for much of the total cooling.
3. Collisional de-excitation reduces the efficiency of the λ1750 emission (§4.2 below).
4. In any likely geometry (§4.3 below), some fraction of the secondary star's radiation escapes along paths through the secondary wind, which is not dense enough for appreciable absorption or emission.

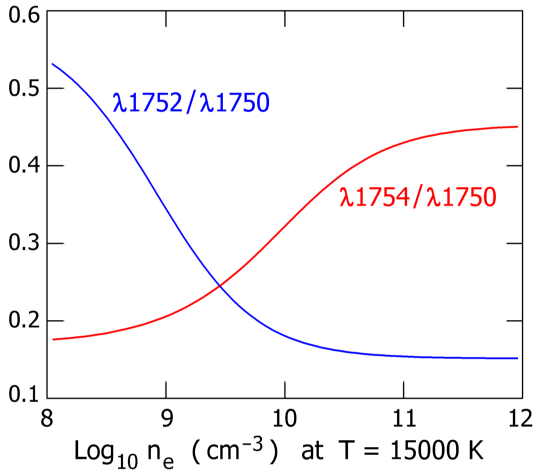

Figure 7. Density-dependent line ratios in the N III] multiplet.

Hence the observed feature is brighter than we would have predicted. Several possible explanations are available. We may have overcorrected F(N III]) for extinction; or the secondary star may be hotter than 40000 K; or FUV photons from the primary star may contribute to the heating via a trick noted in §6 of Humphreys et al. (2008); etc. The main point is that L(N III] λ1750) *appears to be comparable to the maximum attainable value.*

4.2. *Density of the He$^+$, N^{++} zone*

Gas density n_e can help to indicate the location of the He$^+$, N^{++} region, as explained later. Relative intensities of the N III] multiplet components (Table 3) depend approximately on $n_e/T^{0.4}$. We calculated them across a broad density range, using collision strengths and radiative rates reported by Stafford et al. (1994) and Bell et al. (1995). Let us adopt $T = 15000$ K; for other temperatures one can simply multiply each quoted n_e value by $(T/15000\ \mathrm{K})^{0.4}$. Figure 7 shows the brightness ratios of the three most useful lines λ1750, λ1752, λ1754 as functions of density.

Consider the HST data at $t = 2013.82$, the lower panel in Figure 6. Strong peaks near 1748

and 1752 Å represent the λ1750 and λ1754 lines shifted by −300 km s^{-1}, and another member of the multiplet can be discerned near 1747 Å. But there is no peak at 1750 Å corresponding to the λ1752 line. Evidently λ1752 is considerably fainter than λ1754, so Figure 7 immediately indicates $n_e \gtrsim 10^{10}$ cm^{-3}.

In order to be more definite, we need a model for the emission profile. Unrelated absorption lines prevent us from using a deconvolution technique to separate the multiplet structure from the underlying Doppler profile. Instead we estimated the latter by informal trial-and-error experiments. The adopted Doppler profile is shown in the lower panel of Figure 8. We are not confident of the longer-wavelength tail extending to +450 km s^{-1}, but it fits the data reasonably well and its influence on the density estimate is smaller than other uncertainties. The upper panel in Figure 8 shows the resulting total profile for $n_e = 10^9$, 10^{10}, and 10^{11} cm^{-3}, normalized to the major peak. A density of 10^9 cm^{-3} is clearly unsuitable, 10^{11} cm^{-3} gives the best fit, and higher densities are practically indistinguishable from 10^{11} cm^{-3}. The main uncertainty results from irregularities in the underlying fluxes at 1752 Å vs. 1748 Å – i.e., the subtracted "continuum." Assuming that this wavelength region has the same statistical distribution of relative fluxes as the 2000-2200 Å interval (Fig. 2), we estimate that the probabilities of $n_e < 10^{10.0}$ cm^{-3} and $n_e < 10^{10.3}$ cm^{-3} are less than 5% and 22% respectively. A more elaborate analysis, employing a model of the superimposed Fe II and Ni II spectrum, would reduce the uncertainty but is far too lengthy to attempt here.

Collisional de-excitation (Osterbrock & Ferland 2006) reduces the efficiency of N III] λ1750 in the favored density range, because its critical density is $n_c \approx 10^{10.4}$ cm^{-3}. Note, however, that N III] emission is a dominant cooling process and it depends strongly on temperature. If

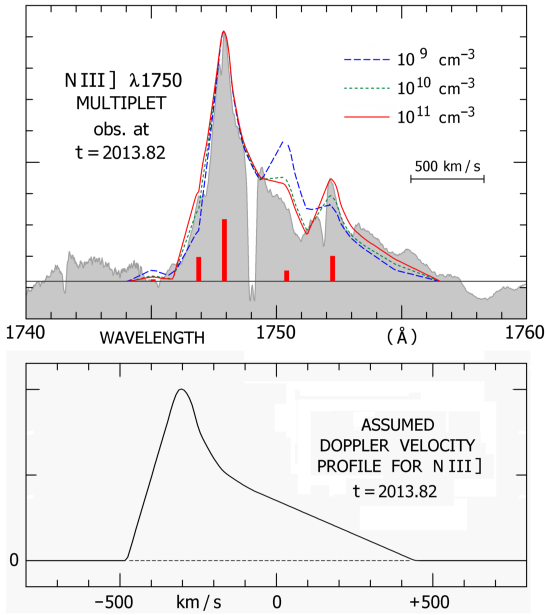

Figure 8. Observed N III] λ1750 profile (shaded), compared to models for densities $n_e = 10^9$, 10^{10}, 10^{11} cm^{-3} (see text). Small vertical bars indicate relative strengths of the multiplet components in the high-density limit. Each model used the Doppler profile shown in the bottom panel.

collisional de-excitation reduces the emission efficiency, then the equilibrium temperature rises so N III] is almost as strong as it would have been without collisional de-excitation. If nearly all of the cooling is due to this feature plus recombination and free-free emission, then the resulting N III] luminosity is reduced by 25% at $n_e \sim 10^{11.2}$ cm^{-3}, and by 50% at $10^{11.7}$ cm^{-3}. Expected temperatures are in the range 13000-23000 K depending on density.

In summary, the N III] λ1750 data favor the density range $10^{10.3} \lesssim n_e \lesssim 10^{11.5}$ cm^{-3}. Lower values produce unsatisfactory multiplet ratios, while higher densities entail excessive collisional de-excitation. The dominant uncertainties are not statistical and they are not caused by imperfections in the data; instead they involve the complex nature of η Car's spectrum. This estimate applies to gas with Doppler velocities near −300 km s^{-1}, because it is based essentially on the peaks seen near 1748 and 1752 Å. Also, of

course, it presumably represents a weighted average for gas that has a range of densities.

4.3. *Location of the N^{++}, and small-scale structure in the shocked region*

Where is this gas located in η Car's wind structure? Figure 9 identifies five different zones, with the primary star at the bottom and the secondary star above it. Every part of this idealized map is inhomogeneous and unstable, but the zones are meaningful regarding ionization states. Regions 1,2,3 are differently ionized parts of the primary wind, which has $v \sim 500$ km s^{-1}. Zone 4 is a shocked region between the two winds, and 5 is the lower-density secondary wind with $v \sim 3000$ km s^{-1}. He^+ and N^{++} may exist in each zone except 2. We tentatively dismiss the inner wind 1 in this problem, because relevant single-star wind models do not produce much N III] emission (Hillier et al. 2001, 2006); but this statement is not absolutely robust and zone 1 will be mentioned again in §4.4. The secondary wind 5 has far too low a density, so we are left with zones 3 and 4.

Zone 3 is the part of the primary wind where helium may be photoionized by the hot secondary star. If the wind had $\dot{M} \approx 10^{-3}$ $M_\odot$ y^{-1} and $v \approx 500$ km s^{-1} (see reviews in Davidson & Humphreys 2012), then the average density there at $t = 2013.82$ would have been $n_e \sim 10^{9.2}$ cm^{-3}, far below the range indicated by the N III] multiplet ratios. Instabilities, however, cause the wind to be inhomogeneous, perhaps with localized density maxima above 10^{10} cm^{-3} (Hillier et al. 2001), and emission lines originate chiefly in those high-density locales. On the other hand, the mass loss rate probably declined well below 10^{-3} $M_\odot$ y^{-1} before 2013, if our interpretation of the secular changes is even partially valid. In summary, region 3 is *probably* not dense enough, but a resourceful skeptic can devise models that avoid this result. The existence or non-existence of this He^+ zone is a non-trivial question, see below.

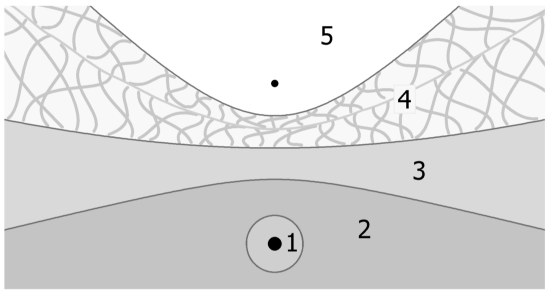

Figure 9. Conceptual arrangement of ionization zones in the two stellar winds. The primary and secondary stars are indicated near the botton and top respectively. The primary wind includes zones 1, 2, and 3, while the less dense secondary wind is zone 5. Region 4 is the complex shocked region. This sketch is *highly* idealized, because every zone is unstable and inhomogeneous.

The shocked region 4 is hostile to simple analysis, and below we shall note reasons to mistrust the numerical simulations that have appeared so far. Boundary 3-4 is not a well-defined shock front, because it is extremely unstable. Consider a sample of gas flowing from region 3 into 4. After being compressed by a factor of about 4 and heated to $T \sim 10^{6.6}$ K, *it is thermally unstable* with a cooling time less than a day (Draine 2011). When the resulting small cloudlets or filaments have cooled to some level below 30000 K, their temperatures stabilize because of UV heating by the two stars. (Here "cloudlet" means, essentially, a local density maximum.) Meanwhile, gas from the secondary wind forms a hot medium in region 4, because its shock front 4-5 has $T \gtrsim 10^8$ K with a cooling time of the order of 0.3 year. Judging from the sound speeds and timescales, pressure equilibrium has a rough validity. Based on pressure quasi-equilibrium, the cooled cloudlets should have densities $n_e \sim 10^{11}$ to 10^{12} cm^{-3}. This picture is obviously consistent with our N III] results.

So far as we know, the morphology of the cooled shocked gas has not yet been modeled with a realistic range of size scales and physical processes. The mass and size of a typical cloudlet may result from one or the other of two effects: (a) Each "clump" in the inhomogeneous primary wind might become a cloudlet, or (b) alternatively, the characteristic size scale for thermal instability may be more decisive: $\ell \sim$ (sound speed) $\times$ (cooling time) ~ 0.03 AU.[3] This suggests a size less than 0.01 AU for a typical cloudlet or filament after it has shrunk due to cooling and surrounding pressure. These condensations might be rapidly disrupted by Kelvin-Helmholtz and/or Rayleigh-Taylor effects, photoionization-driven evaporation, etc., but the observed strong N III] emission with $n_e \sim 10^{11}$ cm^{-3} suggests that this is not the case.

Do they absorb nearly all helium-ionizing photons that enter the shocked region? If not, then a He^+ zone 3 exists in the primary wind. Each cloudlet is opaque at $h\nu \sim 25$ to 30 eV, but photons might pass between them. Therefore, as Mehner et al. (2012) emphasized, the answer depends on sizes, shapes, orientations, and geometrical correlations of the cloudlets. (See the last part of that paper's §3.1.) Imagine a conceptual model with average cloudlet size $s \approx 0.007$ AU. A density compression factor of 100 in each cloudlet implies volume filling factor $\epsilon \approx 0.01$, so the number density of cloudlets would be $N \sim \epsilon/s^3 \sim 10^{4.5}$ AU^{-3}. In order to block almost all photon paths through the shocked region, the mist of cloudlets must extend to a thickness $H \gtrsim 1/s^2N \sim 0.6$ AU perpendicular to boundary 3-4. Given the flow speeds in that region, this extent requires a cloudlet survival time of at least 10 days, which is roughly 10 times the sound-speed crossing time in an individual cloudlet. It is difficult to say whether this survival time is theoretically reasonable.

Clementel et al. (2014, 2015) described elaborate numerical simulations of the shocked flow, but they did not clarify the small-scale morphology. Roughly 10^6 cloudlets are required, so a valid "global" simulation needs at least 10^8 adaptive sample points with small local time steps – far more than the Clementel et al. figures appear to indicate. Those authors' density maps show maxima below $10^{10.3}$ cm^{-3}. Perhaps these are averages over regions large enough to portray in a figure, but *the root of the problem lies at small size scales* $\Delta x \lesssim 0.005$ AU, which are not shown. Moreover, the large compression factors suggest that MHD effects should be included. If some factor prevents compression to the small sizes suggested above, then N III] should have indicated lower densities. Most helium-ionizing photons are probably absorbed in the shocked region as Mehner et al. indicated, but this opinion is not based on numerical simulations, and it has not been proven by them.

4.4. *The puzzling Doppler profile*

Our best-fit distribution of Doppler velocities for N III] (lower panel in Fig. 8) does not resemble simple models. Based on the discussion above, one would expect the N^{++} to flow roughly along pseudo-hyperboloidal surfaces like those sketched in Figure 9 – somewhat analogous to water on an umbrella. At the times of observation, the angle between our line of sight and the umbrella axis was probably in the range 40° to 75°, with us on the

[3] A classical adiabatic shock would produce $T \approx 4\times10^6$ K there, implying a sound speed of about 200 km s^{-1} and cooling time of 2×10^4 s or less. Instabilities, however, may cause the transition 3-4 to be a succession of oblique subshocks. In that case the resulting temperature is lower and the cooling time is shorter.

concave side.[4] In that situation, the positive-velocity tail of the Doppler distribution makes no apparent sense. Assuming that the peak at -300 km s^{-1}, represents the nearest parts of the umbrella, the extreme redshift on the other side should have been less than $+250$ km s^{-1}. Moreover, η Car's He I recombination lines do not have conspicuous long-wavelength wings.

Admittedly we used an informal method to estimate the N III] Doppler profile, but a glance at Figure 6 strongly suggests that the long-wavelength side of the profile extends farther than the short-wavelength side.

We have no good solution to this problem, but here are three speculative ideas. First, the receding N^{++} might be in a distant part of zone 3 in the primary wind. Figure 5b in Mehner et al. (2012) shows that positive velocities may exist there, and the lower density is acceptable because our estimate $n_e \sim 10^{11}$ cm^{-3} really applies only to the peak of the Doppler profile.

A second, less orthodox idea is that N III] might originate in the inner wind (zone 1), contrary to published wind models. The density there has the right order of magnitude, and the energy supply in that region is adequate. The redshifted wing might even be caused by Thomson scattering, since the optical depth there is of order unity in some models (Hillier et al. 2001). A non-spherical wind might achieve such results, in more or less the same vein as Groh et al. (2012a,b, 2015).

As a third possibility, the long-wavelength wing might be the same as the feature noted in §4.5 below.

[4] Quantitative details in this paragraph are based on elementary geometry calculations that are too lengthy and distracting to recite here. They are consistent with most published models of the wind-wind structure. But if the orbit orientation is reversed (Kashi & Soker 2016), then the above discussion has to be modified.

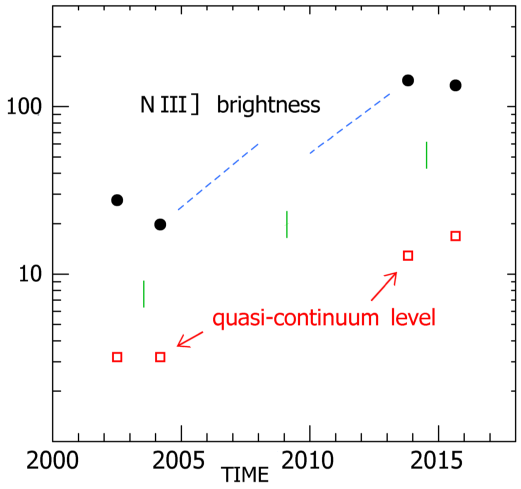

Figure 10. Partial N III] fluxes in range 1746.0–1749.0 Å, expressed in units of 10^{-12} erg cm^{-2} s^{-1} with no correction for extinction. Open squares below are the averages of $f_\lambda(1733)$ and $f_\lambda(1777)$ in Table 2, in units of 10^{-12} erg cm^{-2} Å^{-1}. Vertical marks indicate periastron times. A conjectural discontinuity in the dashed trend line coincides with the 2009 periastron event, cf. Fig. 4.

Arguably the N III] profile "should have" differed between the 2013 and 2015 observations, because the angle between our line of sight and the shock axis differed by about 20° between those two occasions. At least one would expect the -300 km s^{-1} velocity to differ measurably between those orientations. In fact, however, the two profiles in Figure 6 are practically indistinguishable, apart from the variable feature noted below.

4.5. *Variability, and mysterious redshifted emission*

In order to assess the N III] brightness trend without too much absorption-line influence, we integrated f_λ across only the brightest, least affected interval 1746.0–1749.0 Å. Figure 10 shows the results with no extinction corrections nor continuum subtraction. There are two noteworthy findings: (1) The average rate of brightening was 0.17 magnitude per year, about 20% faster than the nearby wavelengths listed in Ta-

ble 2. (2) In both 2002-2004 and 2013-2015, the sample was noticeably fainter after periastron. This deficit was comparable to the luminosity of the anomalous broad feature discussed next.

The $t = 2004.18$ tracing in Figure 5 shows *strong, broad emission around 1755 Å, resembling a dominant emission bump seen during the 2003.5 periastron event.* It also appears, less strongly, in the 2015.67 data (Fig. 6). In view of the innate strength of the N III] multiplet, this feature is almost certainly the λ1750 line with Doppler velocities ranging from +400 to +1200 km s^{-1}. It had an impressive luminosity in 2003-2004, thousands of $L_\odot$. Considering Figures 1 and 9 together, *we cannot easily find a locale for N^{++} with these velocities.* Certain parts of the secondary shock had large positive Doppler velocities in 2004, but the other parts would not, and there is no reason to expect much N^{++} near the secondary shock (§4.3 above).

Perhaps the 1755 Å feature was a remnant of the 2003.5 periastron event that occurred 8 months earlier. In the oldest, and in some respects the most successful interpretation of a periastron event in η Car, $\dot{M}$ temporarily increases so a considerable amount of ejecta moves outward (Zanella et al. 1984; Martin et al. 2006a; Davidson 2012). Since the detailed mechanisms remain unclear, and the secondary star is probably located on the far side of the primary at periastron, we should not be surprised to see large recession velocities in the special ejecta – for example, the broad 1755 Å emission in the middle panel of Figure 5. Can it remain detectable later? By $t = 2014.18$ the special fast ejecta would have been more than 50 AU from the star, and N^{++} would exist there only if there was a clear path for EUV photons from the secondary star to the receding material. This may be possible due to the spiral patterns caused by orbital motion; see Figures in Parkin et al. (2009) and Okazaki et al. (2008), especially the right-hand panel in Figure 3 of Parkin et al. However, this picture would not explain the same feature at 2002.51, if it was weakly present then (Fig. 5).

Evidently we have no satisfying explanation for the broad emission around 1755 Å. Of course the same can be said of some other spectral lines in η Car; but this one has an extraordinary luminosity of the order of 10^4 $L_\odot$. That amount is comparable to the total kinetic energy flow in the wind, and greatly exceeds the total X-ray flux. As Oscar Wilde said, to misplace so much energy almost looks like carelessness.

5. OTHER UNUSUAL EMISSION FEATURES

Various authors have discussed the familiar types of UV stellar wind features seen in η Car (Ebbets et al. 1997; Hillier et al. 2001, 2006; Groh et al. 2012a). Most of those features have deep P Cyg absorption and require sophisticated analyses. Here we note two special emission lines with different characteristics.

Figure 11 shows a grove of bright lines near $\lambda \sim 1900$ Å, as seen in 2002, 2004, 2013, and 2015. Most of the unlabeled features are Fe II, but the lines of interest here are semi-forbidden Si III] and C III] near 1890 Å and 1907 Å.[5] Semi-forbidden lines are useful because their short-wavelength sides are not complicated by P Cyg absorption (see below). From 2002 to 2015 the Si III] and C III] emission generally increased by modest amounts relative to Fe II and Fe III, and also became somewhat narrower. Like the N III] λ1750 peak, their average velocities were close to -300 km s^{-1}.

C III] λ1909 most likely originates in the same gas as N III] λ1750, since the ionization energy for $C^+ \rightarrow C^{++}$ is nearly the same as for $He^0 \rightarrow He^+$. Based only on the nature of the η Car system, we expect the luminosities of N III] and C III] to depend chiefly on the flux of helium-

[5] For a useful list of identifications in η Car's spectrum, see Viotti et al. 1989.

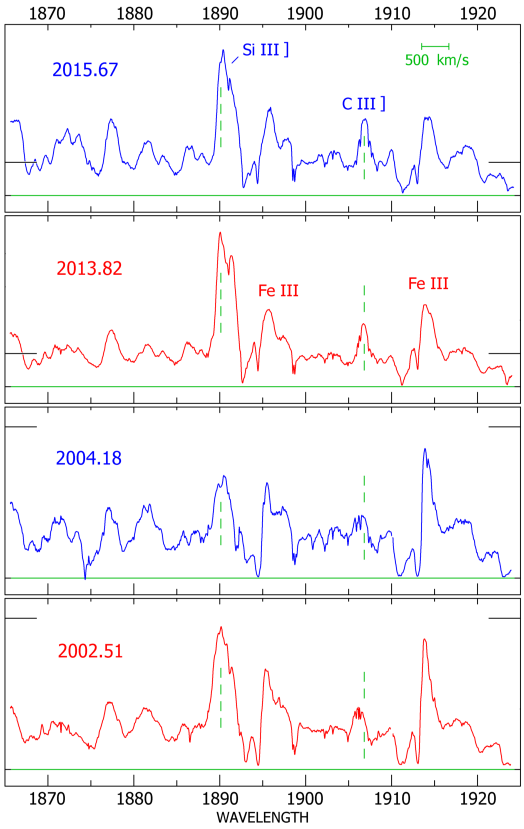

Figure 11. Bright emission lines near 1900 Å in η Car's spectrum. Vertical dashed lines mark Doppler velocities of -300 km s^{-1} for Si III] and C III]. Horizontal marks at the sides indicate $f_\lambda = 10^{-11}$ erg cm^{-1} s^{-1} Å^{-1}, not corrected for extinction.

ionizing photons from the secondary star. However, the critical n_e for collisional de-excitation of C III] is about $10^{9.7}$ cm^{-3}, far below the density range favored in §4.2 above. If $n_e \sim 10^{11}$ cm^{-3}, the observed ratio of C III] to N III] brightness is consistent with an abundance ratio $n_C/n_N \approx 0.1$. The width of C III] λ1909 decreased by a significant amount; its FWHM was roughly 240 km s^{-1} in 2002-2004 but only 160 km s^{-1} in 2013-2015.

Si III] λ1892 should originate in ionization zones of H^+ and He^0. It is the second most conspicuous emission line between 1300 and 2400 Å (Fig. 2), and appears to have at least two components in the range -300 to -120 km s^{-1}. Since it can be formed via an exotic two-photon process (Johansson et al. 2006), this line may convey unique information about the radiation field.

These three semi-forbidden features – N III], C III], and Si III] – share a suggestive velocity trend. Vertical dashed lines in Figure 11 assist in seeing this effect. In 2002 and 2004, the left sides of Si III] and C III] in the figure had wavelengths about 0.6 Å smaller than in 2013 and 2015 – i.e., at the earlier times, some material was approaching us about 100 km s^{-1} faster. A careful comparison of Figures 5 and 6 shows the same effect for the main peak in the N III] multiplet. This velocity change is substantial, even though it appears inconspicuous in the figures. If these were permitted lines, P Cyg absorption would obscure that part of the emission profile.

The above effect might indicate a diminished wind speed; but another, more interesting explanation involves the geometry of the shocks. Consider an emission line that originates in or near the shocked region, in gas flowing roughly parallel to a pseudo-hyperboloid surface like boundary 3-4 in Figure 9. (In §4.4 we called it an umbrella.) Further suppose that our line of sight direction (L.O.S.) was just within the opening angle of the pseudo-hyperboloid at those times – i.e., HST viewed the umbrella obliquely from its concave side. Then the most extreme negative Doppler velocities originate in the region where the flow is almost anti-parallel to the L.O.S. – the near side of the umbrella. Due to gradual weakening of the primary wind, the shock's opening angle should have widened between 2002 and 2015. This trend increased the projection angle between the flow velocity and the anti-L.O.S.; thereby causing the observed effect on the short-wavelength side of the Doppler profile. An increase of the opening angle can have a similar effect on emission from primary wind region 3 in Figure 9, for partially different reasons. If an explanation in this vein is correct, then the total opening angle of the

shocked zone must have increased by at least 20°.

Alternative explanations can be devised, but in any case this velocity effect is one example of the range of questions that a realistic *evolving* model needs to answer.

6. ABSORPTION LINES AND VANISHING MATERIAL

Unlike visual wavelengths, the UV has many permitted transitions from well-populated levels near the ground states. Even small amounts of material can thus form strong absorption features. In η Car's spectrum, they show rapidly declining column densities of several ion species.

Low-ionization absorption lines can occur at large distances from the primary star, and many component velocities have been listed, e.g., by Gull et al. (2006). In the time interval from 2002 to 2015, material flowing outward from η Car could move through distances of the order of 1000 AU. Here we examine only a few definite features seen at t = 2002.51 and 2013.82. Other lines, and the data from 2004 and 2015, are consistent with these findings.

Figure 12 shows Fe II λ1618 absorption. One vertical line marks the lab wavelength and interstellar absorption, while another indicates Doppler velocity −500 km s^{-1}. Very strong absorption extended from −520 to −420 km s^{-1} in 2002, but eleven years later the longer-wavelength half of this interval had become nearly transparent. Column densities also declined in velocity ranges −420 to −360 km s^{-1} and −200 to −100 km s^{-1}. Quantitative assessments would be complicated, but Figure 12 strongly suggests that *the optical depth fell to less than half of its initial value* at most velocities between −470 and −100 km s^{-1}. A similar decrease may have occurred between −520 and −470 km s^{-1}, but if so it was undetectable because the optical depth there remained large.

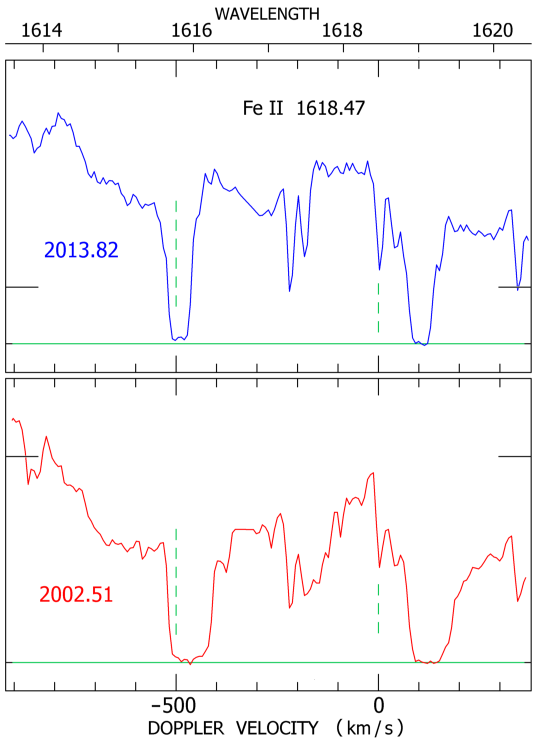

Figure 12. The Fe II λ1618 absorption feature in 2002 and 2013. The zero-velocity absorption is interstellar, and the broad absorption on the right side is a different line. Horizontal marks at the sides indicate $f_\lambda = 4 \times 10^{-12}$ erg cm^{-2} s^{-1} Å^{-1}, not corrected for extinction.

Ni II λ1752, which obscures the N III] profile at 1749 Å, exhibits the same tendencies; compare Figures 5 and 6. This weaker line shows that the amount of material at −350 to −100 km s^{-1} was small compared to the main outflow; but here we emphasize the consistent trends. Near the left edge of Figures 5 and 6 one can see a stronger Ni II line with similar changes. These effects appear to be consistent among the numerous low-ionization UV absorption lines.

The strong Al II λ1671 and Al III $\lambda\lambda$1855,1863 lines have unique qualities for this subtopic. Al^+ coexists with H^0 and Fe^+, while Al^{++} coexists with H^+ and Fe^{++}; but these aluminum ions have much simpler spectra than Fe II and Fe III. Instead of hundreds of confused features, they show only the three lines named above – all arising from ground level, with strong oscilla-

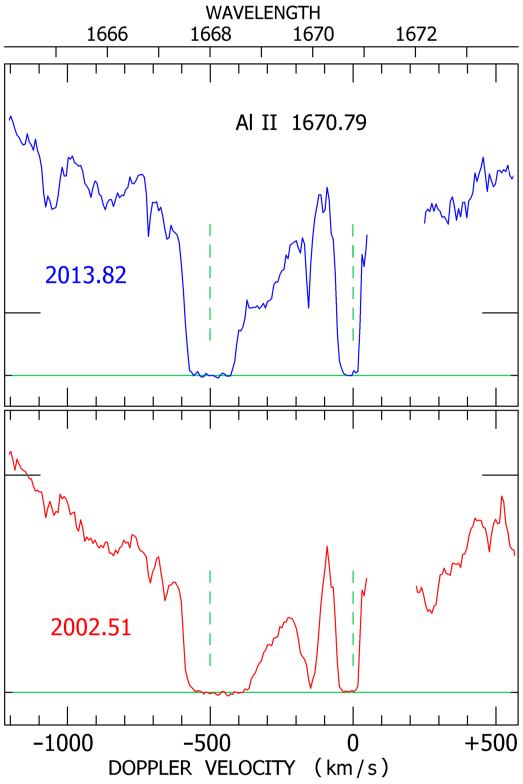

Figure 13. The Al II λ1671 absorption feature in the years 2002 and 2013. Horizontal marks at the sides indicate $f_\lambda = 4 \times 10^{-12}$ erg cm^{-2} s^{-1} Å^{-1}, not corrected for extinction. The data have a gap around 1671.5 Å because two echelle orders did not overlap.

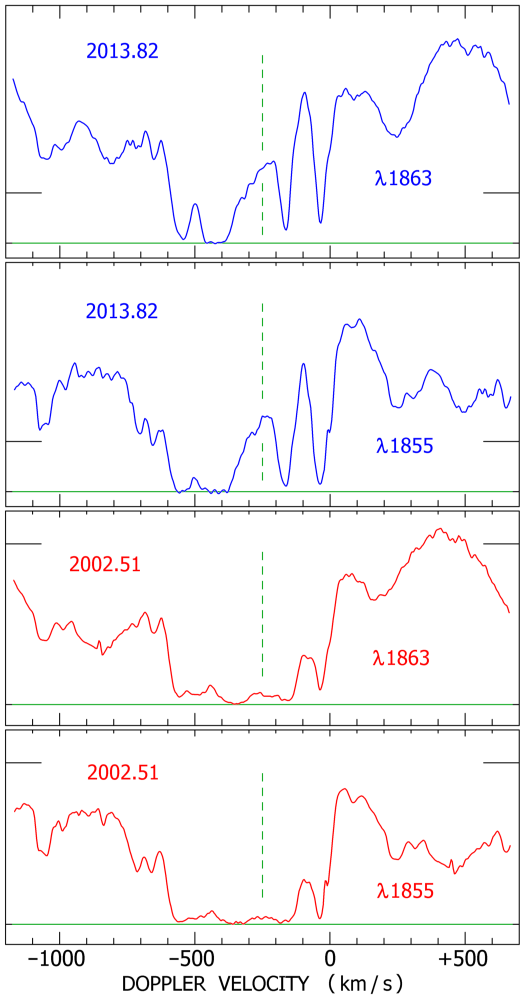

Figure 14. Al III $\lambda\lambda$1855,1863 absorption features seen in 2002 and 2013. The vertical dashed line at -250 km s^{-1} is a guide for noting a subfeature noted in the text. Horizontal markers at the sides indicate $f_\lambda = 4 \times 10^{-12}$ erg cm^{-2} s^{-1} Å^{-1}, not corrected for extinction.

tor strengths $f_{ij} \approx 1.77$, 0.56, and 0.28. Moreover, we can employ the fact that Al III λ1855 is intrinsically twice as strong as λ1863.

These features are shown in Figures 13 and 14, and together they support a particular chain of reasoning. First, the changes in Al II λ1671 were consistent with the Fe II and Ni II trends; absorption decreased at velocities between -420 and -150 km s^{-1}. But the next point is less routine: *The Al III profile in 2013 nearly matched that of Al II in 2002!* (Compare the two figures. The λ1671 tracing has a data gap between +50 and +200 km s^{-1} which probably hides an emission peak, but this does not affect its absorption part.) If we view only this striking resemblance by itself, an obvious interpretation is that some gas became more highly ionized.

However, the Al III lines then lead to an intricate puzzle with potentially major implications. Figure 14 shows a declining, not increasing, column density of Al^{++}. In both 2002 and 2013, that quantity appears to have been *larger* than the Al^{+} column density in the velocity range where a difference can be detected. Now, consider the local brightness maximum (i.e., absorption minimum) between -350 and -200 km s^{-1}, marked by vertical lines in Fig. 14. It was conspicuous in Al II in 2002, and in Al III in

2013. Judging from the overall appearance of this subfeature, one would naively guess that optical depths in that velocity range were moderately small when it was visible. However: both Al III lines represent precisely the same material, and the λ1855 line has an oscillator strength twice as large as for λ1863. Therefore the optical depth $\tau(-250$ km s$^{-1})$ should have been visibly larger in the λ1855 feature. Hence the bump should have been appreciably fainter or less prominent in the Al III λ1855 line compared to λ1863, contrary to observations.

How can we explain this discrepancy? A hypothetical "extra emission" source for the bump would be implausible, since the emissivities differ greatly among the three Al II and Al III lines. The UV halo (Hillier et al. 2006) does not provide a simple explanation, since the two Al III features almost certainly depend on optical depth $\tau(v)$ even if it refers to scattering paths rather than a direct line of sight. If this were not true, then the changing structure in Figure 14 would be very hard to understand. Hence the λ1863 line should appear different from λ1855 even if one cannot predict the details.[6] We propose the following idea, which significantly affects the small-scale geometry of the situation. Suppose that the brightness in these absorption lines between -100 and -350 km s^{-1} depends chiefly on area covering factors, rather than a simple optical depth. In this scenario, part of the projected area is quite dark at those wavelengths because it is optically thick, but another part is almost free of Al^{+} and Al^{++}. Since velocities depend on location, the area covering factor is a function of Doppler velocity. The resulting λ1855 and λ1863 absorption profiles should look alike, as observed. With a few additional assumptions, this concept may partially explain the resemblance between Al II in 2002 and Al III in 2013. Note that this problem involves tiny amounts of material in the stated velocity range. Since the required optical depths imply scarcely more than 0.1% of the expected outflow of aluminum ions in our direction, perhaps we should be surprised that these absorption lines are not dark at all wavelengths from zero to -600 km s^{-1}.

In summary, the above discussion has an obvious underlying thread: *In each absorption feature, at almost every velocity where the optical depths are suitable for detecting a change in column density, a decrease was seen* – and it generally appeared to be of the order of 50% in 11 years, not 10% or 20%. This was not merely an ionization effect, since it includes both Al^{+} and Al^{++}. We can safely assume that these represent most of the aluminum in the absorption-line regions, because the next ionization stage Al^{+3} would require a considerable flux of helium-ionizing photons above 28 eV, at distances far from the star.

7. SUMMARY

Above we have presented an initial survey of some particular HST UV observations of η Car. The results fall into three categories; (1) the star's rapid change of state, (2) morphology of gas flows across a wide range of size scales, and (3) strange features that are not easy to explain.

7.1. *η Car's rapid secular trends*

As noted in §1, we consider the change of state to be the main development in this topic since 2000, because it relates to stellar structure and giant-eruption instability. The UV results outlined in this paper expand the variety of evidence.

Figures 4-6, 10, and 12-14 show many large changes in 2002-2015. Circumstellar UV ex-

[6] The arguments concerning optical depth in §3.1 do not apply here, because they applied only to the general appearance of the Fe II forest with fairly large optical depths. The problems in this section refer, instead, to particular velocity intervals in particular lines, where the optical depths ceased to be large.

tinction decreased by 30% or more along our line of sight (§3 above). Absorption lines indicate that column densities greatly decreased at almost every Doppler velocity where a change would be detectable, and practically vanished at some velocities (§6). This statement includes Al^{++}, not just singly-ionized species. These results are consistent with trends seen at longer wavelengths (Martin et al. 2006b, 2010; Mehner et al. 2010b, 2012; Davidson et al. 2015). In addition, the short-wavelength sides of some emission line profiles shifted between 2004 and 2013 (§5).

If one wishes to explain the observed facts without a major change in η Car's wind, it is necessary to invoke multiple hypotheses. (*a*) Our line of sight must be abnormal in showing major decreases in extinction and line absorption. (*b*) Low-excitation emission lines – whose appearance depends only mildly on viewing direction – must be very sensitive to minor changes in the star and its wind. (*c*) Some third idea must account for spectacular changes in the nature of periastron events from 1998 to 2014 (Davidson et al. 2005, 2015; Mehner et al. 2011b, 2015). (*d*) Velocity profiles of semi-forbidden emission lines (which are not complicated by P Cyg absorption) changed in a particular way noted in §5 above. Each of these points can individually be explained with its own special hypothesis, but we would need to accept all of them together.

It is simpler to deduce, instead, that the stellar wind has diminished by a significant amount – e.g., by roughly 50% since the earliest STIS observations in 1998. That one hypothesis, perhaps including a change in the latitude dependence, can explain nearly all of the observed effects – see Davidson (2012); Mehner et al. (2012); Martin et al. (2006a) and references therein. It strongly suggests a progressive alteration in the stellar radius and/or surface rotation and/or luminosity.

7.2. *Morphology of the emission regions, and numerical simulations*

Eta Car produces an extraordinary amount of N III] λ1750 emission, carrying about as much energy as the entire stellar wind. In §4.2 we used the N III] multiplet ratios to estimate a characteristic gas density $n_e \sim 10^{11}$ cm^{-3}, about two orders of magnitude denser than the primary wind in that vicinity. The high density implies that N III] λ1750 originates in condensations within the colliding-wind shocked region. If our density estimate is seriously wrong, then the N III] and He I emission lines probably occur in a region of the primary wind, zone 3 in Figure 9.

As outlined in §4.3, thermal instability should produce small dense "cloudlets" in the shocked gas. The observed strength of N III] emission, combined with the high density noted above, appears to confirm that this does happen and shows that the cloudlets are not immediately destroyed. Roughly 10^5 to 10^7 cloudlets are required in order to convert most of the secondary star's helium-ionizing photons into N III] and other emission. (Filamentary condensations can be regarded as strings of cloudlets.)

Thus, a valid global model of the shocked region requires more than 10^8 adaptive sample points, with many time steps in the densest locales. A more practical approach, of course, is to produce local simulations of a few hundred cloudlets and combine them with a lower-resolution global flow model – but we are not aware of efforts like that for this object. Published accounts of calculations for η Car's shocked region (e.g. Clementel et al. 2015) have not described the small-scale morphology with densities $n_e \sim 10^{11}$ cm^{-3}.

Realistic models will need additional effects. For instance, both winds are generally thought to be inhomogeneous with dense "clumps." When a clump enters the shocked region, it

may penetrate to a considerable distance like a raindrop falling on soft snow, with a density-enhanced cooling rate. On the secondary wind side, this effect should increase the observable X-ray luminosity and tends to destabilize the shock front. On the primary side, it may determine the size, number, and morphology of cloudlets. A simple filling factor is not adequate for modeling the winds! Meanwhile, since cloudlet formation entails a large density compression factor, magnetic pressures and tensions are likely to be significant. Models of the primary wind are presumably more robust, but similar doubts apply to them as well. They neglect details of the inhomogeneities and other phenomena, and they have simplified geometries. In summary, *existing numerical simulations of η Car's outflows should be regarded as preliminary sketches, not accurate models.*

In §4.4 and §5 we mentioned some details that relate to large-scale morphology. They concern emission line profiles and very likely the opening angle of the shocked region; see those sections. Velocity components within the absorption lines (§6) represent structures in the outflow, but without other information their locations are conjectural.

7.3. *A major unexplained feature*

In 2003-2004, there was a huge amount of N III] emission at velocities around +800 km s^{-1} (§4.5 and Fig. 5). Such a large *recession* velocity is unusual in η Car, and the associated luminosity was extraordinary. We suspect that it was related to a burst of mass ejection in the 2003.5 periastron event (cf. Martin et al. 2006a), but we do not understand its excitation. A similar but weaker feature probably existed in 2015 (Fig. 6), and possibly in 2002.

Helium-ionizing EUV from the hot secondary star is probably the only available energy source for this type of emission, but it requires a clear path between that star and the receding gas on the far side of the primary, with no intervening part of the primary wind. The system's large-scale spiral pattern might provide such a path – see, e.g., the fourth panel in Figure 3 of Parkin et al. (2009). However, only a very small fraction of the secondary star's EUV goes in that direction, so the energy budget is doubtful.

Theorists who enjoy unorthodox models may be able to devise other ways to excite this strange N III] emission. For instance, the latitude-dependent primary star might conceivably have a hot equatorial zone providing EUV. Our main point here, though, is twofold: This feature constitutes a fascinating puzzle, and its high velocities may be significant regarding the periastron spectroscopic event.

Finally, we emphasize two facts. (1) This paper has been essentially a reconnaissance. Many features in the data have been omitted here, and no elaborate models have been employed. (2) HST observed η Car in the UV on several other occasions, ignored here because their orbit phases were unsuitable for our present purpose. *The entire HST UV data set on this object contains enough material for many investigations in a variety of interesting and significant problems.*

— — —

Acknowledgements – We are grateful to A. Mehner for many contributions; she was the P.I. for HST programs GO 13377 and 13789 which obtained the UV spectra in 2013 and 2015. As always, we appreciate the excellent help given by B. Periello and other STScI staff members in planning and scheduling the HST observations. K.I. was supported by Grant-in-Aid for Scientific Research (C) (JSPS KAKENHI Grant Number JP26400227).

REFERENCES

Bell, K.L, Hibbert, A., Stafford, R.P., & Brage, T. 1995, MNRAS, 272, 909

Cardelli, J.A., Clayton, G.C., & Mathis, J.S. 1989, ApJ, 345, 245

Clementel, N., Madura, T.I., Kruip, C.J.H., Icke, V., & Gull, T.R. 2014, MNRAS, 443, 2475

Clementel, N., Madura, T.I., Kruip, C.J.H., Paardekooper, J.-P., & Gull, T.R. 2015, MNRAS, 447, 2445

Davidson, K., Dufour, R.J., Walborn, N.R., & Gull, T.R. 1986, ApJ, 305, 867

Davidson, K., ApJ, 317, 760

Davidson, K., Ebbets, D., Weigelt, G., et al. 1995, AJ, 109, 1784

Davidson, K., & Humphreys, R.M. 1997, ARA&A, 35, 1

Davidson, K., Ebbets, D. Johannson, S., et al. 1997, AJ, 113, 335

Davidson, K., Ishibashi, K., Gull, T.R., & Humphreys, R.M. 1999a, in ASP Conf. Ser. 179, Eta Carinae at the Millennium, 227

Davidson, K., Gull, T.R., Humphreys, R.M., et al. 1999b, AJ, 118, 1777

Davidson, K., Smith, N., Gull, T.R., Ishibashi, K., & Hillier, D.J. 2001, AJ, 121, 1569

Davidson, K., Martin, J., Hummphreys, R.M., et al. 2005, AJ, 129, 900

Davidson, K. 2012, in ASSL 384, Eta Carinae and the Supernova Impostors, Astrophys. & Sp. Sci. Library 384 (ed. K. Davidson & R.M. Humphreys, Springer Media, New York), 43

Davidson, K., & Humphreys, R.M. (eds.) 2012, ASSL 384, Eta Carinae and the Supernova Impostors (Springer Media, New York)

Davidson, K., Mehner, A., Humphreys, R.M., Martin, J.C., & Ishibashi, K. 2015, ApJL, 801:L15

Davidson, K., Ishibashi, K., & Martin, J.C. 2017, RNAAS 1:6

Draine, B.T. 2011, Physics of the Interstellar Medium (Princeton University Press), ch. 34

Ebbets, D.C., Walborn, N.R., & Parker, J.W. 1997, ApJL, 489, L161

Groh, J.H., Hillier, D.J., Madura, T.I., & Weigelt, G. 2012a, MNRAS, 423, 1623

Groh, J.H., Madura, T.I., Hillier, D.J., Kruip, C.J.H., & Weigelt, G. 2012b, ApJL, 799, L2

Groh, J.H., Madura, T.I., Kruip, C.J.H., Paardekooper, J.-P., & Gull, T.R. 2015, MNRAS, 447, 2445

Gull, T.R., Kober, G.V., & Nielsen, K.E. 2006, ApJS, 163, 173

Gull, T.R., Madura, T.I., Teodoro, M., et al. 2016, MNRAS, 462, 3196

Hamann, F. 2012, in ASSL 384, Eta Carinae and the Supernova Impostors, Astrophys. & Sp. Sci. Library 384 (ed. K. Davidson & R.M. Humphreys, Springer Media, New York), 95

Hillier, D.J., Davidson, K., Ishibashi, K., & Gull, T.R. 2001, ApJ, 553, 860

Hillier, D.J., Gull, T.R., Nielsen, K., et al. 2006, ApJ, 642, 1098

Humphreys, R.M., & the HST-FOS Eta Car Team 1999, in ASP Conf. Ser. 179, Eta Carinae at the Millennium (ed. J.A. Morse, R.M. Humphreys, & A. Damineli), 107

Humphreys, R.M., Davidson, K., & Koppelman, M. 2008, AJ, 135, 1249

Humphreys, R.M., & Martin, J.C. 2012, in ASSL 384, Eta Carinae and the Supernova Impostors (ed. K. Davidson & R.M. Humphreys, Springer Media, New York), 1

Johansson, S., Hartman, H., & Letokhov, V.S. 2006, A&A, 452, 253

Kashi, A., & Soker, N. 2016 ApJ, 825:105

Madura, T.I., Gull, T.R., Okazaki, A.T., et al. 2013, MNRAS, 436, 3820

Martin, J.C., Davidson, K., Humphreys, R.M., Hillier, D.J., & Ishibashi, K. 2006a, ApJ, 640, 474

Martin, J. C., Davidson, K., & Koppelman, M. D. 2006b, AJ, 132, 2717

Martin, J. C., Davidson, K., Humphreys, R. M. & Mehner, A. 2010, AJ, 139, 2056

Mehner, A., Davidson, K., Ferland, G.J., & Humphreys, R.M. 2010a, ApJ, 710, 729

Mehner, A., Davidson, K., Humphreys, R.M., et al. 2010b, ApJL, 717:L22

Mehner, A., Davidson, K., Martin, J. C., Humphreys, R. M., Ishibashi, K., & Ferland, G. J. 2011, ApJ, 740:80

Mehner, A., Davidson, K., Humphreys, R.M., Ishibashi, K., Martin, J. C., Ruiz, M. T., & Walter, F. M. 2012, ApJ, 751:73

Mehner, A., Davidson, K., Humphreys, R.M., et al. 2015, A&A, 578, A122
Najarro, F., & Hillier, D.J. 2012, in ASSL 384, Eta Carinae and the Supernova Impostors (ed. K. Davidson & R.M. Humphreys, Springer Media, New York), 67
Okazaki, A.T., Owocki, S.P., Russell, C.M.P., & Corcoran, M.F. 2008, MNRAS, 388, L39
Osterbrock, D.E., & Ferland, G. 2006, Astrophysics of Gaseous Nebulae, chapter 5.6
Owocki, S.P., & Shaviv, N.J. 2016, MNRAS, 462, 345
Parkin, E.R., Pittard, J.M., Corcoran, M.F., Hamaguchi, K., & Stevens, I.R. 2009, MNRAS, 394, 1758
Remmen, G., Davidson, K., & Mehner, A. 2012, ApJ, 773:27
Richardson, N.D., Madura, T.I., St.-Jean, L., et al. 2016, MNRAS, 461, 2540
Stafford, R.P., Bell, K.L., & Hibbert, A. 1994, MNRAS, 266, 715
Teodoro, M., Damineli, A., Heathcote, B., et al. 2016, ApJ, 819:131
Viotti, R., Rossi, L., Casatella, A., Altamore, A., & Baratta, G.B. 1989, ApJS, 71, 983
Walborn, N.R. 1999, in ASP Conf. Ser. 179, Eta Carinae at the Millennium (ed. J.A. Morse, R.M. Humphreys, & A. Damineli), 110
Walborn, N.R. 2012, in ASSL 384, Eta Carinae and the Supernova Impostors (ed. K. Davidson & R.M. Humphreys, Springer Media, New York), 25
Weigelt, G., & Ebersberger, J. 1986, A&A, 163, L5
Weigelt, G., Hofmann, K.-H., Schertl, D., et al. 2016, A&A, 594:A106
Zanella, R., Wolf, B., & Stahl, O. 1984, A&A, 137, 79